Applied Catalysis A, General 580 (2019) 149–157

Contents lists available at ScienceDirect

Applied Catalysis A, General

journal homepage: www.elsevier.com/locate/apcata

Modification of rGO by $B(C_6F_5)_3$ to generated single-site Lewis Acid ≡rGO-O-$B(C_6F_5)_2$ as co activator of nickel complex, to produce highly disperse rGO-PE nanocomposite

Sebastian A. Correa[a], D.E. Diaz-Droguett[c], Griselda B. Galland[b], Thuany G. Maraschin[d], Nara De Sousa Basso[d], Fulya Dogan[e], Rene S. Rojas[a,*]

[a] Laboratorio de Química Inorgánica, Facultad de Química, Pontificia Universidad Católica de Chile, Av. Vicuña Mackenna 4860, Casilla 306, Chile
[b] Instituto de Química, Universidade Federal do Rio Grande do Sul, Av. Bento Gonçalves, 9500, Porto Alegre 91501-970, Brazil
[c] Instituto de Física, Facultad de Física, Pontificia Universidad Católica de Chile, Casilla 306, Santiago, 22 6094411, Chile
[d] Facultade de Química, Pontifícia Universidade Católica do Rio Grande do Sul, Av. Ipiranga 6681, Porto Alegre 90619-900, Brazil
[e] Chemical Sciences and Engineering Division, Argonne National Laboratory, Argonne, IL, 60439, United States

ARTICLE INFO

Keywords:
rGO-PE nanocomposite
rGO-Bis (pentafluorophenyl) borane
In situ activation
Nickel catalysis
Olefin polymerization
Remote activation

ABSTRACT

We investigated the incorporation of reduced graphene oxide (rGO) into branched polyethylene, achieving nanocomposites with different rGO contents. The strategy included the direct reaction between $B(C_6F_5)_3$ (BCF) with rGO (reduced graphene oxide) and demonstrated by XPS, ^{11}B, ^{19}F -MAS NMR, FT-IR the efficient modification of the rGO. The resulting solid contains sites -O-$B(C_6F_5)_2$ capable of acting as co-catalysts in the activation of an (α-iminocarboxamidate)nickel (II) complex. The results show the efficient activation of this nickel catalyst through an exocyclic Lewis acid-base interaction and the subsequent ethylene polymerization. We achieved with this heterogeneous catalytic system activity greater than those previously reported for the BCF-Ni, homogenous system, while the characterization of the black colored polymer generated *in situ*, showed a complete delamination of the rGO. It became the first rGO-$B(C_6F_5)_2$-Ni system fully characterized and capable of delaminate the rGO support by producing a nanocomposite rGO-LLDPE without loss of activity, compared to the homogeneous system. In addition, the polymer contains about 70% of methyl branches and a melting point higher than 125 °C.

1. Introduction

The search for new materials that present new mechanical properties [1–5], thermal, chemical, electrical [6–9], including accelerators for their degradation [10], the research focused mainly on the incorporation of inorganic fillers such as clay, rGO, TiO_2, silica (aerosil), carbon nanotubes, metallic nanoparticles, *etc.* to the polyolefins since even at low concentration, they can strongly change the macroscopic properties of the polymer [11–21]. Traditionally these developments have occurred by melt mixing [3,22,23]. However, due to the low compatibility of the inorganic (polar) and organic (apolar) components, an adequate miscibility and distribution of the components is not achieved. The resulting materials do not reach the expected superior properties, especially when the loading increases by over 10%. One of the most promising approaches for the generation of hybrid organic-inorganic materials with nanocomposite characteristics is *in situ* [20,24–30] polymerization and particularly where the inorganic charge itself is capable of activating an organometallic compound, initiating polymerization at such sites, which favors exfoliation in the case of fillers with laminar nature and allowing access to homogeneous nanocomposites with loading greater than 5%.

Reduced graphene oxide can be also used as a support for organometallic complexes due to the organic functional groups present on its surface which can readily react with commercially available co-catalyst. Dong et al. [28] prepared PP / graphene oxide nanocomposites by a Ziegler-Natta based system, where either BuMgCl or EtMgCl reacted with hydoxyl group present in GO yielding a GO/MgCl solid co-catalyst capable of to support and activated $TiCl_4$. The most common approach widely used to the development of polyolefin/rGO nanocomposites is the impregnation of reduced graphene oxide with methylaluminoxane (MAO), and the subsequent support of a Zr metallocene complex [31–35] or post-metallocene (i. e. cationic Ni system) [36,37].

* Corresponding author.
E-mail address: rrojasg@uc.cl (R.S. Rojas).

https://doi.org/10.1016/j.apcata.2019.05.004
Received 11 January 2019; Received in revised form 29 April 2019; Accepted 2 May 2019
Available online 02 May 2019
0926-860X/ © 2019 Elsevier B.V. All rights reserved.

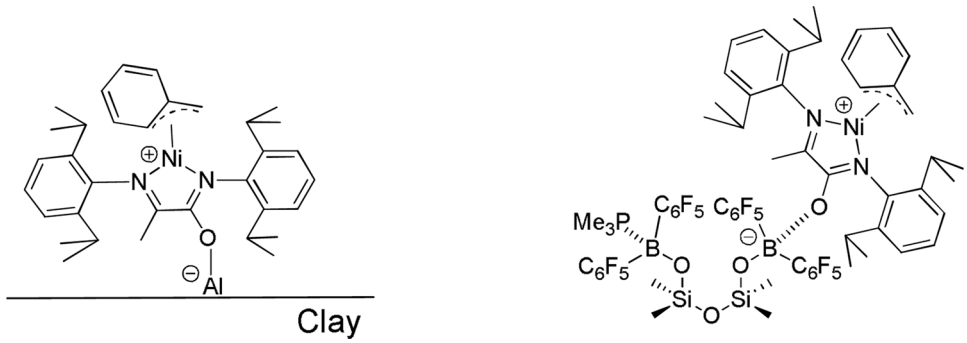

Scheme 1. Examples of heterogeneous single-site coactivator of (α-iminocarboxamidato)nickel(II) complex [47,48].

On the other hand, the effective anchoring of borane Lewis acid co-catalyst on reduced graphene oxide *via* its reaction with the surface organic groups and the subsequent, remote activation by a neutral post-metallocene system based on Ni has not been explored so far. The concept behind this development is the remote activation of the metallic center, by the action of soluble Lewis acid sites such as Zr [38,39] and Ni-based catalyst [40–46] or constitutive of the structure of insoluble inorganic supports [47] or incorporated in these by simple chemical reactions [48].

These sites, by interacting with a basic functionality in the structure of the ligand in the organometallic or coordination complex, increase the electronic deficiency of the metal center, due to the electronic conjugation of said functionality with it, making it sufficiently reactive to coordinate and initiate the polymerization of monomers such as ethylene, propene, norbornene. In Scheme 1 the most representative systems are shown and that until now have been reported to produce organic-inorganic nanocomposites, including rGO-PE.

In this work, we investigated the direct reaction between $B(C_6F_5)_3$ with rGO (reduced graphene oxide) and demonstrated using XPS, ^{11}B, ^{19}F -MAS NMR, FT-IR, the efficient modification of rGO. The resulting solid contains sites -O-$B(C_6F_5)_2$ capable of acting as co-catalysts in the activation of a complex (α-iminocarboxamidato)nickel (II). There is the possibility of using highly active supported versions of these catalysts to incorporate an additive (reduce graphene oxide, clay, silica) that could affect the mechanical, thermal and electrical properties of polymeric nanocomposite materials.

2. Experimental

All manipulations were performed under an inert atmosphere using standard glovebox and Schlenk-line techniques. Toluene, pentane, benzene were distilled from benzophenone ketyl and stored under a nitrogen atmosphere. All reagents were used as received from Aldrich, unless otherwise specified. [N-(2,6-diisopropylphenyl) -2- (2,6-diisopropylphenylimino) propanimidate-κ^2-N,O] Ni(CH_2Ph)PMe_3 **1** was prepared according to a reported procedure [41].

[N-(2,6-diisopropylphenyl)-2-(2,6-diisopropylphenylimino)propanimidate-κ^2-N,O]Ni(n^3-CH_2Ph)- bis(perfluorophenyl)(phenoxy)borane **2** adduct was prepared *in situ* and loaded into Parr reactor. rGO was prepared according to a reported procedure [49]. Chemical shifts are given in parts per million relative to TMS [^1H and ^{13}C, δ($SiMe_4$) = 0] or an external standard [δ ($BF_3{\cdot}OEt_2$) = 0 for ^{11}B NMR, δ($C_6H_5CF_3$) = 0 for ^{19}F NMR]. FT-IR spectra were acquired on a IR tracer-100 Shimadzu using KBr pellets.

2.1. Synthesis of cocatalyst. rGO-O-B(C_6F_5)$_2$

Reduced graphene oxide (rGO) at different amount (10, 20, 50 and 100 mg) and $B(C_6F_5)_3$ (0.04, 0.08, 0.16 and 0.32 mmol, respectively) in benzene were loaded into a Schlenk vessel under nitrogen. The mixture was sonicated for 2 h and refluxed at 80 °C for 48 h. The supernatant was then decanted and the solid washed four times with toluene. Solution state ^{19}F-NMR were recorded at room temperature. Only one product was obtained whose belongs to pentafluorophenylbenzene (For details see Supporting information).

2.2. Synthesis of supported catalyst. rGO-B(C_6F_5)$_2$-Ni

For catalyst support, the desired amount (10, 20, 50 and 100 mg) of rGO-O-$B(C_6F_5)_2$ was placed in a Schlenk vessel with toluene and a solution of nickel complex (**1**) (6 μmol) in toluene was added for each sample using inert atmosphere and was sonicated at room temperature for 8 h. The supernatant was then decanted and the solid washed five times with toluene. In the supernatant, nickel complex was not observed by ^1H and ^{31}P NMR, indicating that it was fully transferred to rGO-O-$B(C_6F_5)_2$.

2.3. Characterization of cocatalyst and supported catalyst

2.3.1. XPS analysis

XPS analysis of rGO, rGO-$B(C_6F_5)_2$, rGO-$B(C_6F_5)_2$-Ni was conducted using a PHI 5000 VersaProbe II XPS system from Physical Electronics, with base pressure approximately 2×10^{-9} torr. Powders were placed in a stainless steel powder sample holder consisting of individual cups, approximately 2 mm in diameter and 1 mm deep. The spectra were obtained using a 100 μm wide, 25 W, Al Kα radiation (hυ = 1486.6 eV) x-ray beam aimed at the center of each cup, with concurrent Ar^+ and electron beam sample neutralization, in Fixed Analyzer Transmission mode. Survey spectra were acquired in the range 0 eV ≤ B.E. ≤ 1400 eV, at 1.0 eV steps, with pass energy of 117.4 eV and 0.5 s per data point total acquisition time. Si2p, P2p, F1s, O1s, and C1s regions were also acquired over appropriate B.E. ranges, at 0.2 eV steps, with pass energy of 23.5 eV and total acquisition times of 6 s per data point for the Si2p and P2p regions, and 3 s per data point for the other regions. Shirley background subtraction and fitting to multiple assymetric peaks were performed on all spectra using the Multipack software from Physical Electronics. The fitted areas of the regions and vendor calibrated sensitivity factors were used to measure the relative concentration (% at.) of the regions of interest.

2.3.2. Solid-state NMR spectroscopy

Solid-state ^{11}B, ^{13}C and ^{19}F MAS NMR experiments were performed at 11.74 T (500 MHz) on a Bruker Avance III HD spectrometer operating at a Larmor frequency of 160.46 MHz, 125.76 and 470.49, respectively. A rotor synchronized echo pulse sequence (π/2 - τ -π - acq.), where $\tau = 1/\nu_r$ (spinning frequency), was used to acquire the ^{11}B and ^{19}F MAS NMR spectra with a 2.5 mm probe at a spinning speed of 30 kHz with pulse widths of 2.6 μs and 1.75 μs and pulse delays of 2s and 5s., respectively. ^{11}B chemical shifts are given relative to $BF_3.Et_2O$, referenced using a secondary reference of 0.1 M H_3BO_3 at 18.8 ppm and a background spectrum collected with same parameters on empty rotor was subtracted from the spectra of the samples. ^{19}F chemical shifts are given

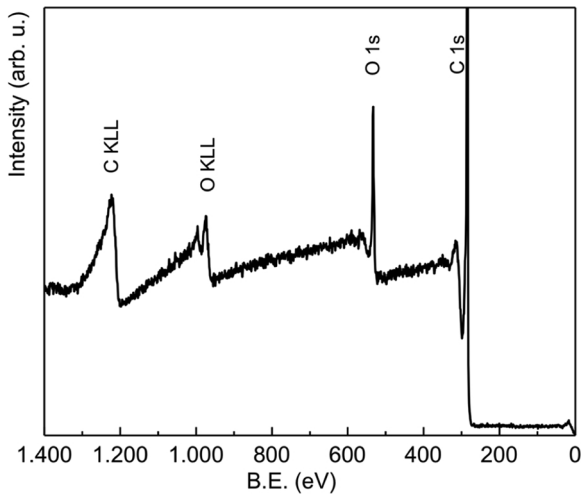

Fig. 1. Broad energy scan XPS spectrum acquired from reduced graphene oxide (rGO).

relative to CCl_3F, referenced using a secondary reference of LiF at −204 ppm. Single pulse experiments were used to acquire ^{13}C MAS NMR spectra with 4 µs pulse width and 10 s pulse delay at a spinning speed of 30 kHz on a 2.5 mm probe. The spectra were referenced to TMS at 0 ppm.

2.4. Polymerization reactions

Polymerization reactions were performed in a 100 ml Parr reactor; the desired amount of cocatalyst rGO-B$(C_6F_5)_2$ and 6 µmol of Ni precursor was loaded into the reactor and 30 g toluene was used as the solvent. The reactions were performed at 25 °C using 100 psi pressure for 10 min. the polymerization reactions were stopped using acetone.

2.5. Polymer characterization

2.5.1. NMR spectroscopy

^{13}C NMR spectra was obtained at 110 °C for both polymer and nanocomposites on a Varian Inova 300, operating at 75 MHz. Polymer samples were prepared in *o*-dichorobenzene and benzene-d_6 (20% v/v) in 5-mm sample tube. The deuterated solvent was used to provide a lock signal. The chemical shifts were referenced internally to the major backbone methylene carbon resonance, which was taken as 30.00 ppm form Me_4Si. Spectra were taken with a 74° flip angle, an acquisition time of 1.5 s, and a delay of 4.0 s. Under those conditions, the spectra are 90% quantitative if only carbon atoms that have a relaxation time (T_1) of less than 2.0 are taken into account [50].

DSC analysis was performed on nanocomposites using a Perkin-Elmer DSC 7 calorimeter. DSC thermograms were recorded at a rate of 10 °C/min in the temperature range of 20 °C–200 °C using samples of 7–10 mg. the melting temperature, T_m, was determined in the second scan, and the degree of crystallinity was calculated from the enthalpy of fusion data obtained from the DSC curves (269 J/g was used for a 100% crystalline material).

2.5.2. Transmission electronic microscopy

High resolution TEM images were obtained at Nanomaterial center, Argonne National Laboratory using the JEM-3010 (a 300 kV transmission electron microscope with a LaB_6 electron source). All samples were prepared by depositing a decalin suspension drop on a copper grid (300 mesh). Impedance measurements of the polymer and nanocomposites were performed according to a reported procedure [51].

3. Results and discussion

3.1. Synthesis and characterization of reduced graphene oxide (rGO) modified with Tris (pentafluorophenyl)borane, [rGO-O-B$(C_6F_5)_2$]

The formation of Lewis acid sites of the type –O-B$(C_6F_5)_2$ in reduced graphene oxide (rGO), whose main reactivity is associated with the presence of oxygen atoms with a different chemical environment [52], whose nature and content depend on the treatments chemical and thermal [27,53] to which they have been subjected during their preparation, makes necessary a micro-structural characterization, with the purpose of directing and optimizing the reactions.

The elemental chemical analysis by Energy Dispersive X-ray Spectroscopy from rGO dried at 200 °C under vacuum conditions for 4 h allowed to estimate an oxidation degree of about 13%, whereas the analysis from its broad energy scan spectrum (Fig. 1) obtained by X-ray photoelectron spectroscopy (XPS) revealed a composition of 89 at% C and 11 at% O.

Fig. 2 shows the curve fit results of high resolution XPS spectra from C 1s and O 1s signals acquired from rGO. The deconvolution of the C 1s signal (Fig. 2a) reveals four curves, the curve of the strongest intensity with a binding energy (B.E.) of 284.3 eV corresponds to the presence of C—C bonds while the curves of weaker intensities are attributed to the presence of the functional groups: epoxy (CO) and hydroxyl (COH) with a B.E of 286.1 eV, Carbonyl (C═O) at 288.7 eV, and Carboxyl (COOH) at 291.5 eV.

On the other hand, the O 1s signal was fitted using two curves (Fig. 2b). The strong signal at 533.1 eV was attributed to the presence of COH groups, whereas the weaker signal at 530.9 eV to CO groups. The O 1s signal fitting allowed differencing and quantifying the presence of

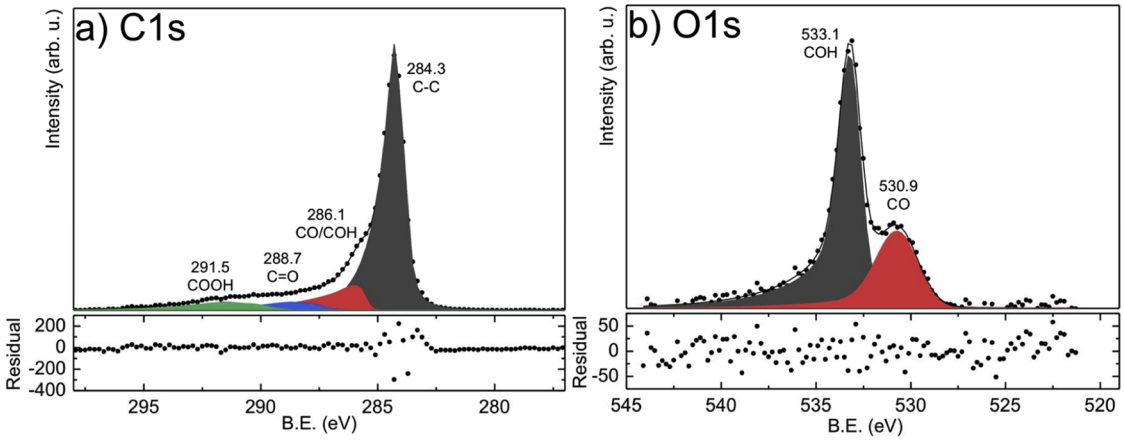

Fig. 2. High-resolution XPS spectra of a) C1s and b) O1s acquired from the rGO.

Table 1
Functional group quantification by XPS.

rGO					
Functional group	C1s	at. %	Functional group	O1s	at. %
C-C	284.3	74	COH	533.1	69
CO/COH	286.1	13	CO	530.9	31
C = O	288.7	6			
COOH	291.5	7			
rGO-O-B(C_6F_5)$_2$					
Functional group	C1s	at. %	Functional group	O1s	at. %
C-C	284.4	67	COH	533.1	33
COH	286.2	5	CO	532.4	67
CO	288.2	19			
COOH/CF	291.5	9			

these two oxygen functional groups (CO and COH) since from the C 1s fitting results both groups belonged to a same curve at 286.1 eV, as shown in Fig. 2a. Quantification of the presence of the different functional groups from rGO was performed with the curve fitting results of the C 1s and O 1s high-resolution signals. These results are displayed in Table 1 revealing that the higher concentration of oxygen is attributed to the presence of the COH and CO groups, followed by the COOH and C=O groups. Additionally, the FT-IR spectrum of this material corroborates the presence of the OH, C=O and C=C functional groups (signals at frequencies of; 3425, 1728, 1535 cm^{-1} respectively) (see Supporting information).

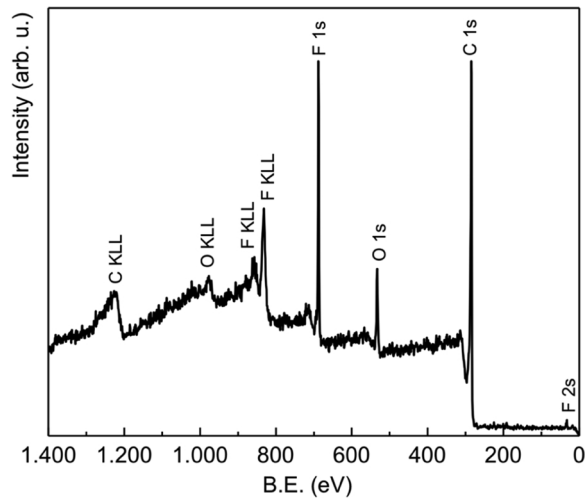

Fig. 3. Broad energy scan XPS spectrum acquired from rGO-O-B(C_6F_5)$_2$.

Due to the higher content of hydroxy groups, the control reaction between phenol and B(C_6F_5)$_3$ was carried out in order to study the viability of direct protonolysis. The reaction (Eq. 1) leads only to the formation of the boronic ester bis(perfluorophenyl)(phenoxy)borane (PhOB(C_6F_5)$_2$). For details of the characterization, see Supporting information (Fig. S1a,b).

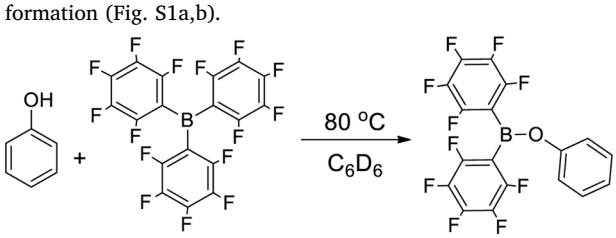

(1)

This result suggests that direct protonolysis between B(C_6F_5)$_3$ and rGO is favorable. Additionally, the background on the heterogeneous reaction of SiOH groups of silica with B(C_6F_5)$_3$ to form Si-O-B(C_6F_5)$_2$ recently reported by Scott et al., [48] proceeded to the chemical modification of rGO with B(C_6F_5)$_3$.

The control reaction was carried out in a schlenk vessel using deuterated benzene (Eq. (2)). The heterogeneous mixture (50 mg of rGO and 0.16 mmol of B(C_6F_5)$_3$ in 2 ml of C_6D_6) was subjected to ultrasound for 2 h at 30 °C and then kept at 80 °C for 48 h under gentle agitation, both processes under nitrogen atmosphere. The ultrasound led to delaminate the graphene sheets making accessible the hydroxyl functional groups located within the laminar structure, increasing their reactivity toward B(C_6F_5)$_3$. The reaction was followed by ^{1}H and ^{19}F-NMR in solution. The multiplet observed in the spectrum of ^{1}H-NMR at 5.8 ppm accounts for the formation of (C_6F_5H) product of the reaction of B(C_6F_5)$_3$ and the OH groups of the rGO.

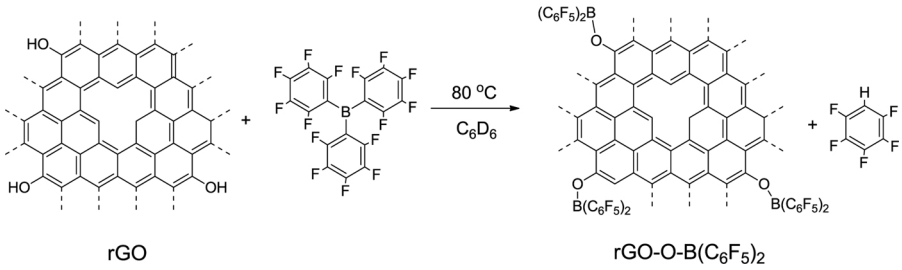

(2)

The ^{19}F-RMN spectrum (Fig. S2) corroborates the above, observing 3 signals at −138, −145 and −161 ppm, corresponding to the F at *ortho, para and meta* positions of the C_6F_5H ring. As expected, the ^{11}B-RMN spectrum did not show any resonance peak, indicative of any by-product or soluble species that contains boron. The results are 100% coincident with the comparison pattern indicated above (Eq. (1)) and therefore indicates that the expected chemical reaction occurred. In order to corroborate the presence of the Lewis -O-B(C_6F_5)$_2$ acid site in the solid (rGO), this was characterized by XPS, MAS-NMR of ^{11}B, ^{19}F, FT-IR. By means of XPS analysis acquired from rGO-O-B(C_6F_5)$_2$ (Fig. 3) was identified the photoelectron signals of Fluorine (F1s and F 2s) coming from the C_6F_5 groups besides the corresponding signals associated with O and C. The quantification performed revealed a composition of 80 at% C, 8 at% O y 12 at% F from this sample. Fig. 4 shows the curve fitting results of the high-resolution spectra of C 1s and O 1s acquired from the rGO-O-. B(C_6F_5)$_2$. Fig. 4a shows an appreciable change of the C 1s signal shape as compared with the one acquired from rGO (see Fig. 2a). The C 1s signal was fitted also using four curves associated to the presence of C—C bonds at 284.4 eV, and the functional groups COH at 286.2 eV, CO at 287.2 eV and the last curve at 291.5 eV was attributed to the presence of both COOH and CF groups. In this spectrum is possible to differentiate the curves associated to the COH and CO groups. Due to the reaction of B(C_6F_5)$_3$ with the COH functional groups from the rGO (Eq. (2)), the Boron atoms present in the rGO-O-B (C_6F_5)$_2$ molecule form a B—O bond where the boron atom attracts towards itself electronic density from the oxygen atom due to its higher Lewis acidity. The presence of this B—O bond generates a change in the chemical environment of the carbon that participate in the C—O bond

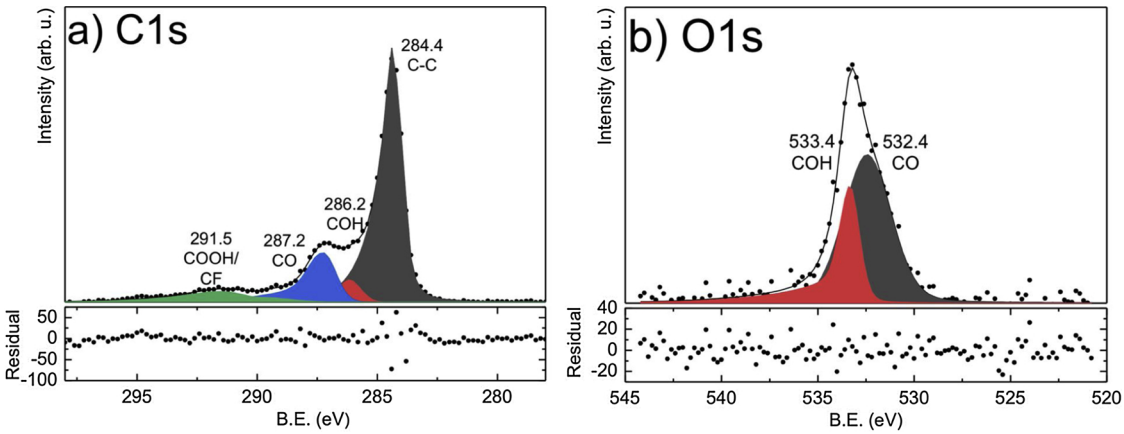

Fig. 4. High resolution XPS spectra of a) C1s and b) O1s acquired from rGO-O-B$(C_6F_5)_2$.

present in rGO-O-B$(C_6F_5)_2$ leading to a shift of its B.E towards higher values, as revealed by Fig. 4a where a B.E. of 287.2 eV was assigned to CO groups unlike the 286.1 eV assigned in the Fig. 2a. On the other hand, the Fig. 4b also shows a change in the O 1s signal where the curve associated with the presence of CO groups also is shifted towards a higher B.E. value of 532.4 eV, i.e, 1.5 eV higher than the value assigned for this type of functional group in the O 1s signal acquired from rGO, as shown in Fig. 2b. This B.E. shift is also attributed to the presence of the B—O bonds in the rGO-O-B$(C_6F_5)_2$. The B.E at 533.4 eV attributed to the presence COH groups only underwent a slight shift of 0.3 eV as compared with the value assigned for the rGO, as shown in Fig. 2b. Table 1 also contains the quantification of the functional groups from rGO-O-B$(C_6F_5)_2$ performed with these high resolution XPS spectra (Fig. 4). This Table reveals that the presence of the COH groups dropped from 66% to 33% indicating the reactivity of these functional groups present in rGO with the C_6F_5 groups, as suggested by Eq. (2).

This can be also observed by FT-IR (Fig. S4), the stretching band of the hydroxyl groups at 3425 cm^{-1} diminished after reaction with B$(C_6F_5)_3$. Additionally, in order to demonstrate unambiguously the reactivity of the hydroxyl groups, a complete reaction of this group with a stoichiometric amount of B$(C_6F_5)_3$ was done. After reaction with B$(C_6F_5)_3$, the peak at 3425 cm^{-1} disappeared, indicating unequivocally that the in the modification process. hydroxyl groups can be completely removed (Fig. S5). On the other hand, Table 1 shows that the presence of CO groups increases from 19% to 67% due to the formation of CO—B bonds in the rGO-O-B$(C_6F_5)_2$ molecule.

The results set forth above demonstrate the reactivity of the OH groups to B$(C_6F_5)_3$. However, they do not give information regarding the degree of boron coordination in the new site created. This is why a study was conducted by ^{11}B MAS NMR, as shown in Fig. 5, the boron spectrum shows a wide signal between 40 and -20 ppm, with a peak at 13 ppm and a quadrupolar constant of approximately 2.6 MHz. Which is consistent with an expected tri-coordinate boron and characteristic of solid materials. These values are close to those reported for boron-modified silica, [48,54] species BO_3 in borosilicates, [55,56] B$(OH)_3$ in zeolite β doped with boron [57] or in MCM-41 modified with boron [58].

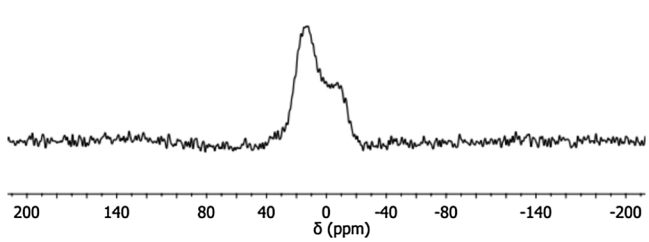

Fig. 5. Solid-state ^{11}B MAS NMR spectrum of rGO-O-B$(C_6F_5)_2$.

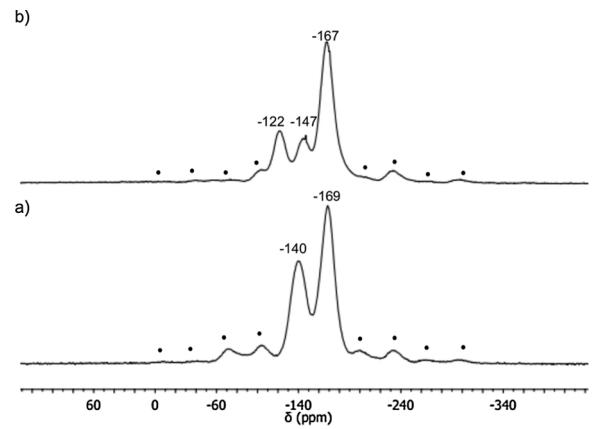

Fig. 6. Solid-state ^{19}F MAS NMR a) rGO-O-B$(C_6F_5)_2$ and b) rGO-B$(C_6F_5)_2$-Ni. (•, spinning sidebands).

Fig. 6(a) shows the ^{19}F MAS NMR spectrum for the rGO-O-B$(C_6F_5)_2$ solid. Two signals are observed at −140 and −169 ppm. As in solution, it would be expected to have 3 set of signals for group C6F5 corresponding to the positions *ortho, para and meta*. Whose ranges are: o-F ($-125 < \delta < -140$ ppm), p-F ($-140 < \delta < -155$ ppm), and m-F ($-155 < \delta < -140$ ppm). However, due to the width of the resonance peak (−120 to −155 ppm), the fluorine *o* and *p* may overlap at the peak centered at 140 ppm.

3.2. Synthesis and characterization of Ni-catalyst supported over rGO-O-B$(C_6F_5)_2$, [rGO-B$(C_6F_5)_2$-Ni]

Having corroborated the modification of the rGO with B$(C_6F_5)_3$ and the subsequent generation of the site -OB$(C_6F_5)_2$, tri-coordinated (Eq. (2)) and added to the activation test of the complex [N-(2,6-diisopropylphenyl)-2-(2,6-diisopropylphenylimino)propanimidato-κ^{2}N,O]Ni$(CH_2Ph)PMe_3$ **1** (Bazan´s Precatalyst (8a)) [41] with bis(perfluorophenyl)(phenoxy)borane **2**, (Entry 1, Table 2), which showed an activity of 430 Kg / mol_{Ni} h, this value is 30% lower than that obtained when activating the precatalyst with B$(C_6F_5)_3$. Based on these results, heterogenization of the complex **1** was carried out on rGO-O-B$(C_6F_5)_2$, (Eq. (3)). The reaction was carried out in a controlled atmosphere chamber (N_2), adding to a toluene suspension of 50 mg of rGO-O-B$(C_6F_5)_2$ a red solution of complex **1** (6 μmol) in the same solvent. The mixture was kept at room temperature under sonication for 8 h. This facilitates the interaction of all -OB$(C_6F_5)_2$ sites present in the rGO sheets, making possible their Lewis acid-base interaction with complex **1**. The intercalated nickel catalyst can react with ethylene, leading to the polymerization inside the rGO sheets.

Table 2
In situ polymerization results*.

Entries	rGO-B(C_6F_5)$_2$[a]	Yield[b]	% rGO[c]	% rGO[d]	A[e]	T_m[f]	X_c[g]	B[h] (mol%)	Methyl (mol%)	Long (C_6) (mol%)
1	–	0.85	–	–	430	129	30	1.6	1.6	–
2	10	1.31	0.8	0.2	660	125	22	5.0	3.4	1.6
3	20	1.33	1.5	1.8	670	126	28	4.8	4.5	0.3
4	50	1.54	3.2	3.7	780	127	25	6.3	4.6	1.7
5	100	2.03	4.9	4.8	1,030	125	23	7.8	6.8	1.0

* Content of Ni precursor 6 μmol.
[a] Amount of rGO-B(C_6F_5)$_2$ in mg.
[b] Performance in grams.
[c] Percentage of incorporated rGO, determined by mass balance.
[d] Percentage of incorporated rGO, determined by TGA.
[e] Activity in Kg PE / (mol Ni h).
[f] Melting temperature determined by DSC.
[g] crystallinity determined by DSC.
[h] Total branches [50].

When the solid was decanted, the complete discoloration of the solution was observed, indicative of the transfer of complex **1** to the solid (rGO-O-B(C_6F_5)$_2$), which was recovered by centrifugation, washing with fresh toluene and drying under vacuum. The characterization by FT-IR, ^{19}F,^{13}C MAS NMR and XPS of the resulting solid was focused on corroborating the presence of the nickel complex in the rGO-O-B(C_6F_5)$_2$.

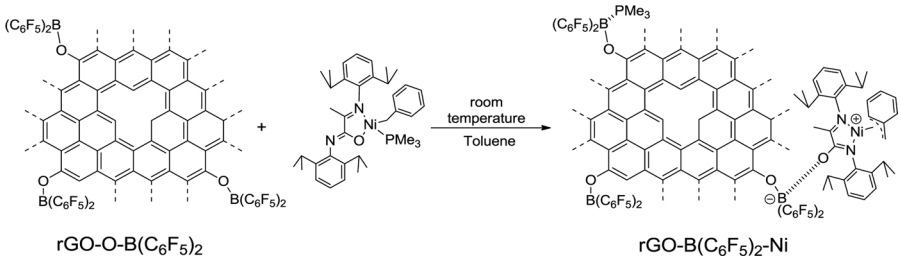

(3)

Comparing the FT-IR (Figs. S5 and S6) spectra a) rGO-O-B(C_6F_5)$_2$ between b) rGO-B(C_6F_5)$_2$-Ni. The band at 1381 cm^{-1} (Fig. S5) was assigned to *stretching* B—O [59]. The most intense bands at 1519 y 1465 cm^{-1} indicated the presence of an aryl group bonded to boron (stretching B—C, C—B—C wagging, and ring-breathing) [60]. Upon reaction of **1** with rGO-O-B(C_6F_5)$_2$ (Fig. S6), the *stretching* C—H of isopropyl fragment are observed at 2900 – 2800 cm^{-1}. The position of C_6F_5 ring-breathing mode at 1519 cm^{-1} is essentially unaffected by the presence of **1**. However, the bands at 1465 cm^{-1} (which includes a contribution from *stretching* B—O) and 1381 cm^{-1} shifts to 1458 and 1375 cm^{-1}, respectively. This shift is consistent with the coordination of Lewis base to a strong Lewis acid site [61,62].

In the same way, when comparing the ^{19}F MAS NMR spectra for rGO-O-B(C_6F_5)$_2$ and rGO-B(C_6F_5)$_2$-Ni, in the latter, unlike the observed for rGO-O-B(C_6F_5)$_2$, they are identified clearly the 3 multiplets (Fig. 6b) of resonances at −120, −145 and −168 ppm associated with the fluorine atoms *ortho, para, and meta* respectively.

This is due to the change in the coordination of boron from tri to tetra-coordinated which limits the rotation of the fluorinated rings, allowing their differentiation. In addition, ^{19}F chemical shift is a sensitive probe to the boron coordination number. The chemical shift for the F atoms in position *p*, is associated with the change of coordination number around Boron [63]. ^{13}C MAS NMR (Fig. 7) shows two chemical shifts for rGO-O-B(C_6F_5)$_2$ which correspond to graphene (carbons with

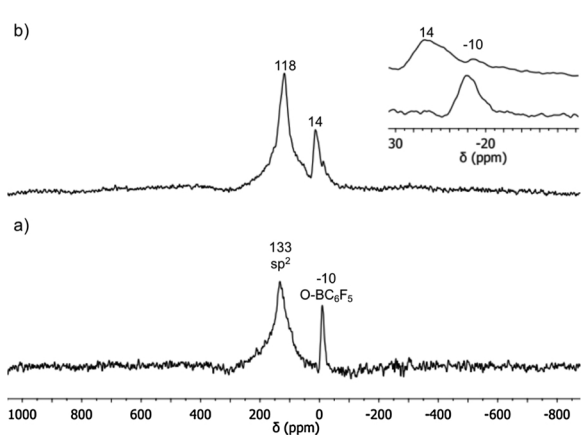

Fig. 7. Solid-state ^{13}C MAS NMR, a) rGO-O-B(C_6F_5)$_2$, and b) rGO-B(C_6F_5)$_2$-Ni.

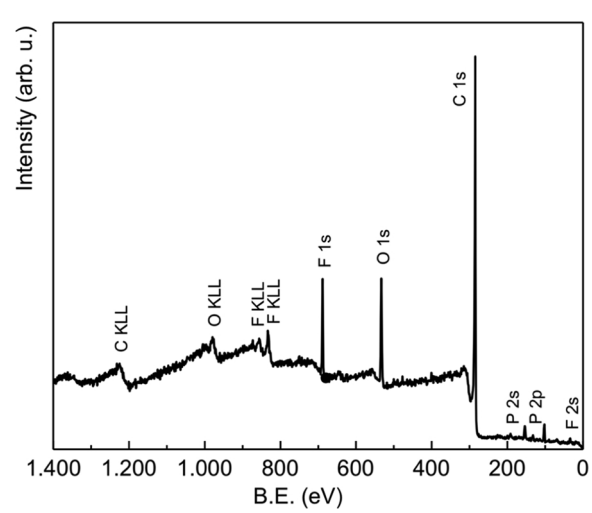

Fig. 8. Broad energy scan XPS spectrum acquired from rGO-B(C_6F_5)$_2$-Ni.

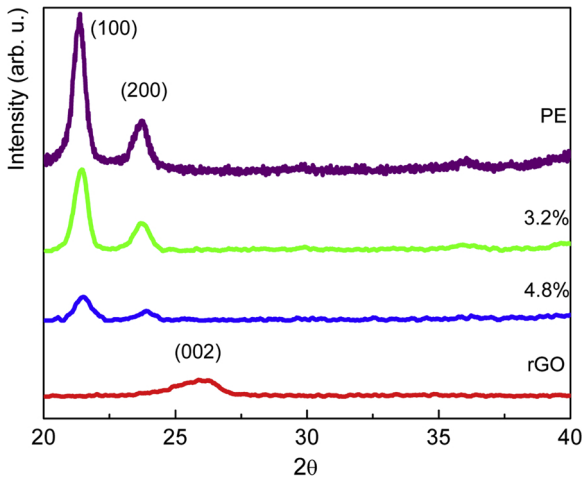

Fig. 9. XRD patterns of PE, rGO and nanocomposites.

sp^2 hybridization) [64,65] 132 ppm and the carbons bound to boron (B-C_6F_5) to −9 ppm (Fig. 7a). By supporting the precatalyst **1** a displacement of the signal corresponding to (O-B(C_6F_5)$_2$) is observed at 14 ppm (Fig. 7b) which is indicative of the Lewis acid-base interaction with the precatalyst. In addition, it can also be observed that there is a small signal that remains at −9 ppm, because not all Lewis acid sites created are being occupied. Finally, a displacement from 133 to 118 ppm was observed for the sp^2carbons. This shows that the coordination of the precatalyst has an electronic effect on the whole structure of graphene, the removal of the electronic density by the boron center and, in turn, its conjugation with the graphitic structure leads to an increase in the protection of the atoms of carbon.

On the other hand, the analysis performed from the broad energy scan XPS spectrum acquired from rGO-B(C_6F_5)$_2$-Ni (Fig. 8) reveals that the B.E. values of C 1s, O 1s and F 1s are similar to the ones obtained from rGO-B(C_6F_5)$_2$. However, it is possible to observe from the Fig. 9 photoelectron signals coming from phosphorus, which are due to the phosphine (PMe_3), as indicated by Eq. (3). No nickel signals were detected from this XPS spectrum, likely due to its low atomic concentration as compared to the presence of the C, O or F atoms.

3.3. Reactivity studies of rGO-B(C_6F_5)$_2$-Ni

The reactivity studies were carried out in a Parr autoclave reactor in 30 g of toluene at a pressure of 100 psi and 25 °C for 10 min. The reference catalytic system for this study corresponds to the reaction in homogeneous phase using the same precatalyst **1** (6 μmol) activated with 5 equivalent of PhOB(C_6F_5)$_2$ **2**. The activity reached a moderate value and 30% lower than that reported for **1** + B(C_6F_5)$_3$ under the same reaction conditions, which may be associated with the lower Lewis acidity of PhOB(C_6F_5)$_2$ respect to B(C_6F_5)$_3$. The polymer obtained has a low crystallinity consistent with a melting point of 129 °C and methylated ramifications that reach 1.6 mol% (Entry 1, Table 2). The reactivity results of the heterogeneous system rGO-B(C_6F_5)$_2$-Ni were obtained taking 6 μmol of Ni precursor and adding 10, 20, 50 and 100 mg of the cocatalyst rGO-B(C_6F_5)$_2$. For each sample, the nickel content was kept constant and the reaction conditions were the same to the homogenous reactions (reference system Table 2). The data show an activity on average 35% higher compared to the reference (Entry 2 and 3). This difference is accentuated by increasing the content of rGO-B (C_6F_5)$_2$, reaching a value 2.4 times higher when 100 mg of rGO-B (C_6F_5)$_2$ (Entry 5) is used.

The behavior of these systems is contrary to what was observed when heterogenizing metallocene and postmetalocene compounds where the activity decreases [66,67] and it may be associated with the fact that the previous modification of rGO with B(C_6F_5)$_3$ ultrasound-assisted favors the separation of the macro sheets and in addition the -O-B(C_6F_5)$_2$ removes traces of impurities present in the solid, making the subsequent activation of the nickel complex more effective (this last step is carried out immediately prior to the polymerization reaction).

In addition, the laminar structure of graphene protects the metallic center, making it more sterically hindered, and causing the Ni center to be more electrophilic [47]. This is confirmed by the study by ^{13}C-MAS NMR (Fig. 7a,b), the chemical shifts indicate a removal of electronic density of the catalyst by the boron center, which, being in resonance with the graphitic structure, disturbs the electronic environment of all support. The increase in activity as the rGO content increases can be explained due to the ratio B/Ni is greater, this favors the exocyclic activation of the Nickel complex and therefore results in a greater number of active sites exposed to ethylene during the polymerization process. Additionally, the higher content of Boron acts as a scavenger in the reaction medium, reducing the possibility of deactivation of the Nickel active sites.

The microstructure of the nanocomposite materials (rGO-PE) was studied by ^{13}C-NMR, and the results are shown in Table 2. An increase in the total branching degree is observed at higher rGO content; this result is expected due to that the graphene sheets increase the steric hindrance around the *o-aryl* substitutes [68]. It is well known that the microstructure of PE produced by Ni catalysts is strongly influenced by the steric environment of *o-aryl* substitutes, ethylene pressure and temperature [69]. Microstructural analysis shows the increase in methyl branches as well as long chain branches (C_6), although the latter does not show a trend.

The melting temperature is strongly determined by the type of branches present in PE, the increase in the density of methyl branches, as well as the increase of long chains decreases the lamellar thickness of crystal structure that lowers the melting point of the polymer (Entries 2–5, Table 2) [70]. As expected, this increase in branches is reflected in

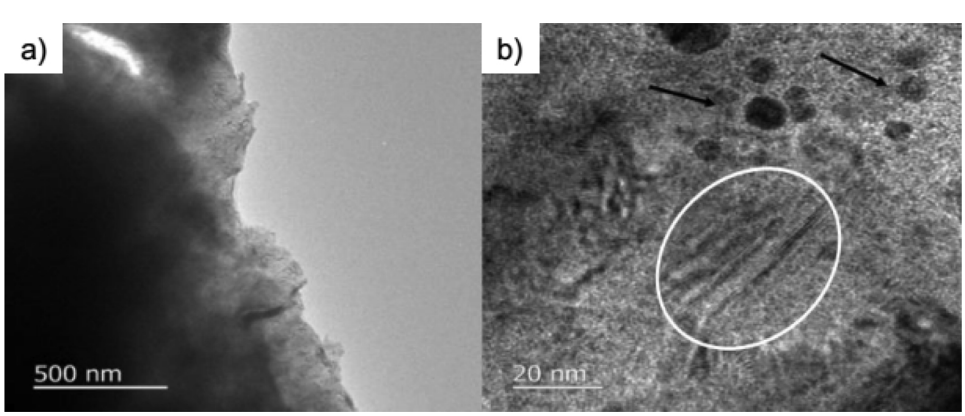

Fig. 10. Nanocomposite TEM micrographs 4.9% rGO at different magnification.

the decrease of Xc with respect to the reference value (Entry 1, Table 2). In addition, the decrease in crystallinity reflects the negative effects of the rGO sheets as a nucleating agent, this result it has been reported by others research groups [31,71,72].

To evaluate the dispersion of the rGO sheets within the polymer matrix, the powder X-ray diffraction (p-XRD) technique was used. Fig. 10 shows the XRD patters of PE, rGO and the nanocomposites 3.2 and 4.9 wt. % rGO. The PE has two peaks at 21.38 and 23.78°, corresponding to the planes (110) and (200), respectively, [73] that can also be seen in the nanocomposites. The diffraction at 25.89° is typical for rGO [9]. As can be seen in the diffractogram, none of the nanocomposites presents the peak of rGO. This confirms the good dispersion within the polymer matrix.

To verify if the nanocomposites have a homogeneous dispersion or not, Transmission Electron Microscopy (TEM) was used. Fig. 10 shows two micrographs at different magnification for the nanocomposite with 4.9% rGO. In image a) the good dispersion of rGO within the polymer matrix is evidenced, the black areas correspond to rGO and the light areas to PE. Magnifying the image shows, the presence of rGO in the shape of small lines (Fig. 10b, circle) scattered and there are some agglomerates (black arrows) of nanocrystals of rGO. These results, together with those obtained by means of p-XRD, confirm the good dispersion of rGO within the PE matrix.

Finally, the capacity of these nanocomposites to conduct electricity through Impedance Spectroscopy was studied. For this, films were prepared by means of a hydraulic press at 130 °C and then their conductivity was measured. The conductivity value for rGO is $1{,}7 \times 10^{-1}$ S cm^{-1}, while the conductivity value found for PE was, ~10^{-13} S cm^{-1}, typical value for an electrical insulator. All measured nanocomposites listed in Table 2 showed no variation in conductivity, remaining in the same order of magnitude that PE. We compared these results with rGO used in similar work reported by Galland et al. [35] in those studies the percolation threshold has a value of 5.5 wt%. Some works suggested that a slight aggregation of the conductor filler may improve the maximum electrical conductivity [74], however, in the *in situ* polymerization, the PE grew around the filler, improving the dispersion but enveloping the rGO with a layer of insulating material. In our case no aggregate was observed, probably due to the low content of rGO in the polymer matrix so the system was not capable of to create a conductive network.

4. Conclusion

The reaction of $B(C_6F_5)_3$ with reduced graphene oxide at 80 °C is a simple protonolysis, transforms surface hydroxyl groups into -O-B$(C_6F_5)_2$ site. XPS and FT-IR analysis indicates the reactivity of hydroxyl groups toward $B(C_6F_5)_3$. Solid-state ^{11}B MAS NMR spectroscopy confirm that -O-B$(C_6F_5)_2$ site is tri-coordinate. These sites are strongly Lewis acid, based on studies by solid-state ^{19}F and ^{13}C MAS NMR spectroscopy demonstrating the Lewis acid-base interaction between -O-B$(C_6F_5)_2$ and nickel complex **1**. The new heterogeneous Lewis acid support, rGO-B$(C_6F_5)_2$, is capable to act as a cocatalyst for Ni (II) complexes in olefin polymerization. Through *in situ* polymerization, it was possible to obtain highly dispersed nanocomposites; the microstructural analysis of the polymer evidenced the influence of the support of the polymer microstructure. Finally, the ability to conduct electricity was studied, however, due to the low loading level; it was not possible to increase the conductivity. In a future work will study the mechanical and electrical properties of the nanocomposites with higher levels of filler.

Acknowledgments

This work was supported by FONDECYT project No. 1161091, CONICYT (grant no 21140118), Chile. Argonne National Laboratory´s work was supported by the U.S. Department of Energy, Office of Science, office of Nuclear Physics, under contract No. DE-AC02-06CH11357.

Appendix A. Supplementary data

Supplementary material related to this article can be found, in the online version, at doi:https://doi.org/10.1016/j.apcata.2019.05.004.

References

[1] T. Kuila, S. Bose, A.K. Mishra, P. Khanra, N.H. Kim, J.H. Lee, Polym. Test. 31 (2012) 31–38.
[2] R. Asmatulu, W.S. Khan, R.J. Reddy, M. Ceylan, Polym. Compos. 36 (2015) 1565–1573.
[3] M. El Achaby, A. Qaiss, Mater. Des. 44 (2013) 81–89.
[4] M.E. Achaby, F.-E. Arrakhiz, S. Vaudreuil, Ael K. Qaiss, M. Bousmina, O. Fassi-Fehri, Polym. Compos. 33 (2012) 733–744.
[5] Y. Chen, Y. Qi, Z. Tai, X. Yan, F. Zhu, Q. Xue, Eur. Polym. J. 48 (2012) 1026–1033.
[6] H. Hu, G. Zhang, L. Xiao, H. Wang, Q. Zhang, Z. Zhao, Carbon 50 (2012) 4596–4599.
[7] J. Du, L. Zhao, Y. Zeng, L. Zhang, F. Li, P. Liu, C. Liu, Carbon 49 (2011) 1094–1100.
[8] P.-G. Ren, Y.-Y. Di, Q. Zhang, L. Li, H. Pang, Z.-M. Li, Macromol. Mater. Eng. 297 (2012) 437–443.
[9] G. Pavoski, T. Maraschin, M.A. Milani, D.S. Azambuja, R. Quijada, C.S. Moura, N. de Sousa Basso, G.B. Galland, Polym. J. 81 (2015) 79–86.
[10] W. Hu, J. Zhan, X. Wang, N. Hong, B. Wang, L. Song, A.A. Stec, T.R. Hull, J. Wang, Y. Hu, Ind. Eng. Chem. Res. 53 (2014) 3073–3083.
[11] F. Ciardelli, S. Coiai, E. Passaglia, A. Pucci, G. Ruggeri, Polym. Int. 57 (2008) 805–836.
[12] S.N. Tripathi, G.S. Srinivasa Rao, A.B. Mathur, R. Jasra, RSC Adv. 7 (2017) 23615–23632.
[13] M. Kato, A. Usuki, N. Hasegawa, H. Okamoto, M. Kawasumi, Polym. J. 43 (2011) 583–593.
[14] L. Zheng, R.J. Farris, E.B. Coughlin, Macromolecules 34 (2001) 8034–8039.
[15] A. Zohrevand, A. Ajji, F. Mighri, Polym. Eng. Sci. 54 (2014) 874–886.
[16] F. Daver, E. Baez, R.A. Shanks, M. Brandt, Compos. Part A 80 (2016) 13–20.
[17] H. Skaff, M.F. Ilker, E.B. Coughlin, T. Emrick, J. Am. Chem. Soc. 124 (2002) 5729–5733.
[18] N. Guo, S.A. DiBenedetto, P. Tewari, M.T. Lanagan, M.A. Ratner, T.J. Marks, Chem. Mater. 22 (2010) 1567–1578.
[19] L.A. Fredin, Z. Li, M.A. Ratner, M.T. Lanagan, T.J. Marks, Adv. Mater. 24 (2012) 5946–5953.
[20] D.R. Paul, L.M. Robeson, Polym. J. 49 (2008) 3187–3204.
[21] N.D. McDaniel, M.P. McDaniel, L. Balzano, D.E. Resasco, J. Appl. Polym. Sci. 111 (2009) 589–601.
[22] Y. Lin, J. Jin, M. Song, J. Mater. Chem. 21 (2011) 3455–3461.
[23] H. Kim, S. Kobayashi, M.A. AbdurRahim, M.J. Zhang, A. Khusainova, M.A. Hillmyer, A.A. Abdala, C.W. Macosko, Polym. J. 52 (2011) 1837–1846.
[24] M.A. Milani, D. González, R. Quijada, N.R.S. Basso, M.L. Cerrada, D.S. Azambuja, G.B. Galland, Compos. Sci. Technol. 84 (2013) 1–7.
[25] A. Tchernook, M. Krumova, F.J. Tölle, R. Mülhaupt, S. Mecking, Macromolecules 47 (2014) 3017–3021.
[26] A. Kheradmand, A.R. S.a, F. Khorasheh, M. Baghalha, H. Bahrami, Polym. Adv. Technol. 26 (2015) 315–321.
[27] T. Kuilla, S. Bhadra, D. Yao, N.H. Kim, S. Bose, J.H. Lee, Prog. Polym. Sci. 35 (2010) 1350–1375.
[28] Y. Huang, Y. Qin, Y. Zhou, H. Niu, Z.-Z. Yu, J.-Y. Dong, Chem. Mater. 22 (2010) 4096–4102.
[29] W. Kaminsky, Front. Chem. Sci. Eng. 12 (2018) 555–563.
[30] T. Hees, F. Zhong, T. Rudolph, A. Walther, R. Mülhaupt, Adv. Funct. Mat. 27 (2017) 1605586.
[31] H. Zhang, J.-H. Park, K.-B. Yoon, Compos. Sci. Technol. 154 (2018) 85–91.
[32] M. Alexandre, M. Pluta, P. Dubois, R. Jérôme, Macromol. Chem. Phys. 202 (2001) 2239–2246.
[33] B. Choi, J. Lee, S. Lee, J.-H. Ko, K.-S. Lee, J. Oh, J. Han, Y.-H. Kim, I.S. Choi, S. Park, Macromol. Rapid Commun. 34 (2013) 533–538.
[34] J.S. Lee, Y.S. Ko, Catal. Today 232 (2014) 82–88.
[35] F. de, C. Fim, J.M. Guterres, N.R.S. Basso, G.B. Galland, J. Polym. Sci. Part A: Polym. Chem. 48 (2010) 692–698.
[36] M. Khoshsefat, S. Ahmadjo, S.M.M. Mortazavi, G.H. Zohuri, RSC Adv. 6 (2016) 88625–88632.
[37] L. Zhang, E. Castillejos, P. Serp, W.-H. Sun, J. Durand, Catal. Today 235 (2014) 33–40.
[38] A.R. Cabrera, Y. Schneider, M. Valderrama, R. Fröhlich, G. Kehr, G. Erker, R.S. Rojas, Organometallics 29 (2010) 6104–6110.
[39] R.S. Rojas, B.C. Peoples, A.R. Cabrera, M. Valderrama, R. Fröhlich, G. Kehr, G. Erker, T. Wiegand, H. Eckert, Organometallics 30 (2011) 6372–6382.
[40] J.D. Azoulay, R.S. Rojas, A.V. Serrano, H. Ohtaki, G.B. Galland, G. Wu, G.C. Bazan, Angew. Chem. Int. Ed. 48 (2009) 1089–1092.
[41] B.Y. Lee, G.C. Bazan, J. Vela, Z.J.A. Komon, X. Bu, J. Am. Chem. Soc. 123 (2001) 5352–5353.
[42] B.M. Boardman, J.M. Valderrama, F. Muñoz, G. Wu, G.C. Bazan, R. Rojas, Organometallics 27 (2008) 1671–1674.

[43] B.Y. Lee, X. Bu, G.C. Bazan, Organometallics 20 (2001) 5425–5431.
[44] R.S. Rojas, G.B. Galland, G. Wu, G.C. Bazan, Organometallics 26 (2007) 5339–5345.
[45] O.S. Trofymchuk, D.V. Gutsulyak, C. Quintero, M. Parvez, C.G. Daniliuc, W.E. Piers, R.S. Rojas, Organometallics 32 (2013) 7323–7333.
[46] B.M. Boardman, G.C. Bazan, Acc. Chem. Res. 42 (2009) 1597–1606.
[47] S.L. Scott, B.C. Peoples, C. Yung, R.S. Rojas, V. Khanna, H. Sano, T. Suzuki, F. Shimizu, Chem. Commun. (2008) 4186.
[48] Y.-J. Wanglee, J. Hu, R.E. White, M.-Y. Lee, S.M. Stewart, P. Perrotin, S.L. Scott, J. Am. Chem. Soc. 134 (2012) 355–366.
[49] G. Pavoski, T. Maraschin, M.A. Milani, D.S. Azambuja, R. Quijada, C.S. Moura, N. de Sousa Basso, G.B. Galland, Polym. J. 81 (2015) 79–86.
[50] G.B. Galland, R.F. de Souza, R.S. Mauler, F.F. Nunes, Macromolecules 32 (1999) 1620–1625.
[51] I.R. Rodrigues, M.M. de Camargo Forte, D.S. Azambuja, K.R.L. Castagno, React. Funct. Polym. 67 (2007) 708–715.
[52] M. Fang, K. Wang, H. Lu, Y. Yang, S. Nutt, J. Mater. Chem. 19 (2009) 7098–7105.
[53] V. Georgakilas, M. Otyepka, A.B. Bourlinos, V. Chandra, N. Kim, K.C. Kemp, P. Hobza, R. Zboril, K.S. Kim, Chem. Rev. 112 (2012) 6156–6214.
[54] A. Agarwala, T. Subramani, A. Goldbourt, D. Danovich, R. Yerushalmi, Angew. Chem. Int. Ed. 52 (2013) 7415–7418.
[55] L.-S. Du, J.F. Stebbins, J. Non-Cryst. Solids 315 (2003) 239–255.
[56] L.-S. Du, J.F. Stebbins, J. Phys. Chem. B 107 (2003) 10063–10076.
[57] H. Koller, C. Fild, R.F. Lobo, Microporous Mesoporous Mater. 79 (2005) 215–224.
[58] A. Sayari, I. Moudrakovski, C. Danumah, C.I. Ratcliffe, J.A. Ripmeester, K.F. Preston, J. Phys. Chem. 99 (1995) 16373–16379.
[59] S. Socrates, Infrared and Raman Characteristic Group Frequencies: Tables and Charts, 3rd edition, Wiley, 2004.
[60] G.D. Sorarù, N. Dallabona, C. Gervais, F. Babonneau, Chem. Mater. 11 (1999) 910–919.
[61] B.A. Morrow, A. Devi, J. Chem. Soc. Faraday Trans. 1 (68) (1972) 403–422.
[62] K. Possemiers, P.V.D. Voort, E.F. Vansant, J. Chem. Soc. Faraday Trans. 92 (1996) 679–684.
[63] T. Beringhelli, D. Donghi, D. Maggioni, G. D'Alfonso, Coord. Chem. Rev. 252 (2008) 2292–2313.
[64] I.A. Vacchi, C. Spinato, J. Raya, A. Bianco, C. Ménard-Moyon, Nanoscale 8 (2016) 13714–13721.
[65] H. He, T. Riedl, A. Lerf, J. Klinowski, J. Phys. Chem. 100 (1996) 19954–19958.
[66] J.R. Severn, J.C. Chadwick, Dalton Trans. 42 (2013) 8979.
[67] G.G. Hlatky, Chem. Rev. 100 (2000) 1347–1376.
[68] S. Park, S.W. Yoon, K.B. Lee, D.J. Kim, Y.H. Jung, Y. Do, H.J. Paik, I.S. Choi, Macromol. Rapid Commun. 27 (2006) 47–50.
[69] D.P. Gates, S.A. Svejda, E. Oñate, C.M. Killian, L.K. Johnson, P.S. White, M. Brookhart, Macromolecules 33 (2000) 2320–2334.
[70] B.K. Bahuleyan, M.A. Atieh, S.K. De, M.J. Khan, M.A. Al-Harthi, J. Polym. Res. 19 (2012) 9744.
[71] A.D. Todd, C.W. Bielawski, Polym. J. 54 (2013) 4427–4430.
[72] H.-X. Zhang, J.-H. Park, E.-B. Ko, Y.-K. Moon, D. Lee, Y.-M. Hu, X.-Q. Zhang, K.-B. Yoon, RSC Adv. 6 (2016) 73013–73019.
[73] J.-W. Shen, W.-Y. Huang, S.-W. Zuo, J. Hou, J. Appl. Polym. Sci. 97 (2005) 51–59.
[74] J.R. Potts, D.R. Dreyer, C.W. Bielawski, R.S. Ruoff, Polym. J. 52 (2011) 5–25.